

## **Development and validation of a bespoke phantom to test accuracy of Cobb angle measurements**

Faisal Alrehily<sup>1,2</sup>

Peter Hogg<sup>2</sup>

Martin Twiste<sup>2</sup>

Safora Johansen<sup>3,4</sup>

Andrew Tootell<sup>2</sup>

<sup>1</sup> *College of Applied Medical Sciences, Taibah University, Medina 42353, Saudi Arabia.*

<sup>2</sup> *School of Health and Society, University of Salford, Salford M5 4WT, United Kingdom.*

<sup>3</sup> *Oslo Metropolitan University, Faculty of Health Sciences, Norway.*

<sup>4</sup> *Department of Oncology, Division of Cancer Medicine, Surgery and Transplantation, Oslo University Hospital, Radiumhospitalet, Oslo, Norway.*

## **Abstract**

**Introduction:** Adolescent idiopathic scoliosis (AIS) is a spinal deformity that causes the spine to bend laterally. Patients with AIS undergo frequent X-ray examinations to monitor the progression of the disorder by through the measurement of the Cobb angle. Frequent exposure of adolescents poses the risk of radiation-induced cancer. The aim of this research was to design and build a bespoke phantom representing a 10-year-old child with AIS to allow optimisation of imaging protocols for AIS assessment through the accuracy of Cobb angle measurements.

**Method:** Poly-methyl methacrylate (PMMA) and plaster of Paris (PoP) were used to represent human soft tissue and bone tissue, respectively, to construct a phantom exhibiting a 15° lateral curve of the spine. The phantom was validated by comparing the Hounsfield unit (HU) of its vertebrae with that of human and sheep. Additionally, comparisons of signal-to-noise ratio (SNR) to those from a commercially available phantom. An assessment of the accuracy of the radiographic assessment of the Cobb angle measurement was performed.

**Results:** The HU of the PoP vertebrae was 628 (SD= 56), human vertebrae was 598 (SD= 79) and sheep vertebra was 605 (SD= 83). The SNR values of the two phantoms correlated strongly ( $r = 0.93$  ( $p = 0.00$ )). The measured scoliosis angle was 14 degrees.

**Conclusion:** The phantom has physical characteristics (in terms of spinal deformity) and radiological characteristics (in terms of HU and SNR values) of the spine of a 10-year-old child with AIS. This phantom has utility for the optimisation of x-ray imaging techniques in 10 year old children.

**Implications for practice:** A phantom to investigate new x-ray imaging techniques and technology in the assessment of scoliosis and to optimise currently used protocols.

## Introduction

Scoliosis is defined as a deformity of the spine in the form of a lateral curve (i.e. in the coronal plane). Adolescent idiopathic scoliosis (AIS) is the most common type of scoliosis, representing 75–90% of cases<sup>1,2</sup> and its causes are unknown.<sup>3</sup> The United Kingdom (UK) Scoliosis Association estimates that 3–4 per 1000 children in the UK are diagnosed with AIS. In most cases, AIS does not require treatment and, instead, is observed until patients mature around 18-21 years old.

Confirmation of AIS diagnosis requires radiological examination of the spine. X-ray images are used to determine the severity and flexibility of the curve and skeletal maturity.<sup>2,4</sup> The progression of the curve is monitored in follow-up X-ray imaging sessions by taking Cobb angle measurements, and imaging can take place at 3–12-month intervals, depending on the curve severity, patient age and management plan.<sup>5</sup> It is estimated that patients with mild AIS can have three radiographs per year, and patients with severe AIS can have up to 12 radiographs per year.<sup>5</sup>

Due to the frequent exposure to X-rays, patients with AIS are at increased risk of developing radiation-induced cancer later in life. This is mainly because of their young age, in that patients are expected to have long lifespans, and radiation-induced cancer has a long latency period that can be measured in decades.<sup>6–8</sup> Therefore, the adherence to ALARP (as low as reasonably practicable) principle is essential to optimise radiation dose and hence reduce the radiation risk to patients.

Optimising an imaging protocol for Cobb angle measurements requires using a phantom to avoid exposing humans to radiation. However, such phantoms typically have a normal spine, which does not fit the purpose of testing the accuracy of Cobb angle measurements. An alternative approach is to use a scoliotic spine model similar to that used by Chung *et al.*<sup>9</sup>,

shown in Figure 1. However, their phantom lacks soft tissue, meaning the effect of scatter radiation is missing. Therefore, the aim of our research was to build a phantom with a scoliotic spine and soft tissue substitute to give it the same bony anatomy appearance and attenuation characteristics of a scoliotic patient. The phantom can then be used to optimise the imaging of patients with AIS or test the accuracy of Cobb angle measurements when using new imaging techniques. This paper explains how we designed, constructed and validated our phantom.



Figure 1: The phantom used by Chung et al. (2018).

## **Method**

Poly-methyl methacrylate (PMMA) and plaster of Paris (PoP) were used for constructing the phantom, representing soft tissue and bone tissue, respectively<sup>10</sup>. The construction of the phantom consisted of two steps: (1) building a scoliotic spine model to be used as a template for the phantom, and (2) building the phantom.

## Designing a template for the phantom

The phantom was built based on CT images of the spine of 10-year old female; however, the images were for a patient without scoliosis and CT images of AIS patients were not obtainable because CT scanning is not widely used for assessing scoliosis due to the high radiation dose. Instead, CT images were taken of a scoliotic spine model (Figure 2) that was constructed from a standard (i.e. non-scoliotic) skeleton model to which a scoliotic curve was added. This was done by using a standard anatomical skeleton model (Figure 2). The vertebrae were removed from the model (Figure 3) and the supporting aluminium rod replaced with one that had been reshaped to exhibit a 15° curvature. (Figure 5):



Figure 2: Standard skeleton model used as a template for constructing a scoliotic spine model.

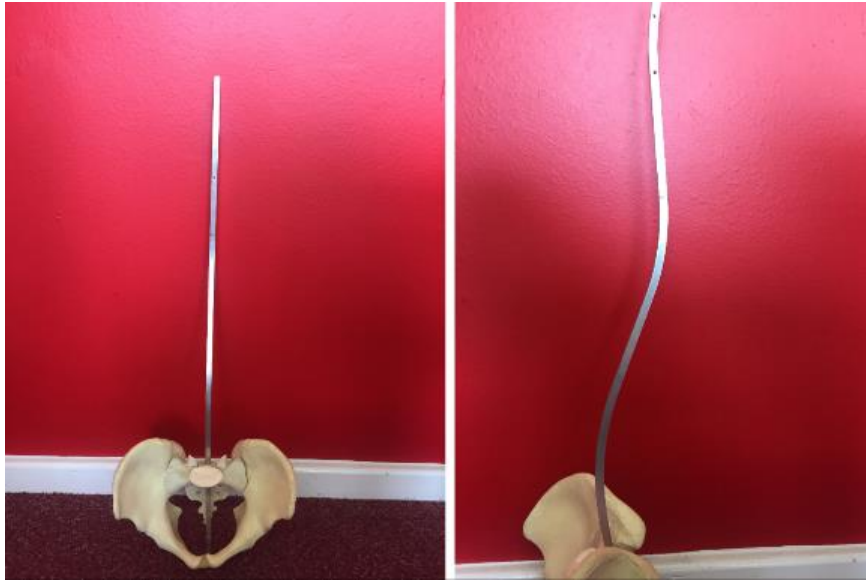


Figure 3: Original rod in the frontal (left) and lateral (right) views.

The curve of this scoliotic spine model was based on the most common magnitude of curve in AIS, which is 10–20°<sup>11–18</sup>, and hence the median angle [ $\beta$ ] of 15° was chosen for this model (half of this was the angle [ $\alpha$ ] 7.5°, and the length (C) of 0.15 m was half of the spine's 0.3 m full length) (Figure 4). Bending the rod to an angle [ $\beta$ ] of 15° required calculating the offset (A) between the aluminium rod when it is straight (representing a straight spine) and then bent (representing a scoliotic spine), as followed:

1) Calculating the radius (R) of the circle that defines the curve of the scoliotic spine model:

$$R = \frac{C}{\sin \alpha} \Rightarrow R = \frac{0.15m}{\sin 7.5^\circ} = 1.15m$$

2) Calculating  $\epsilon$ :

$$\epsilon = \delta - \gamma \Rightarrow \epsilon = \frac{180^\circ - \alpha}{2} - (180^\circ - 90^\circ - \alpha) \Rightarrow \epsilon = \frac{180^\circ - 7.5^\circ}{2} - (180^\circ - 90^\circ - 7.5^\circ) \Rightarrow \epsilon \approx 4^\circ$$

3) Calculating A:

$$\tan \epsilon = \frac{A}{C} \Rightarrow A = \tan \epsilon \times C \Rightarrow A = \tan 4^\circ \times 0.15m \Rightarrow A \approx 0.01m = 1cm$$

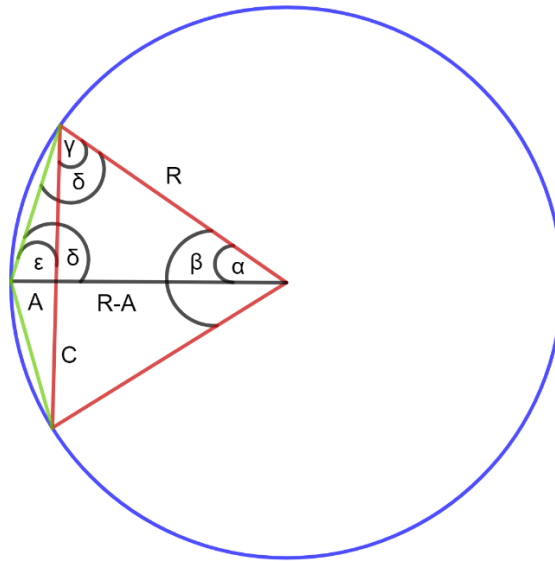


Figure 4: Diagram illustrating the amount of bending ( $A$ ) needed to produce a scoliotic spine with an angle ( $\beta$ ) of  $15^\circ$ .

Therefore, the rod was bent laterally by 1 cm (Figure 5). Then, the labelled vertebrae were mounted in their original order on the bent rod, and the remaining bones of the torso were added too (Figure 6). With the scoliotic spine model ready, the next step was to image it using CT (Toshiba Aquilion; Toshiba Medical Systems, Tokyo, Japan). The vertebrae came from a standard skeleton, and were therefore of adult size. It was therefore necessary to scale down the images to match the vertebral size of a 10-year-old girl from the CT images (approximately 2 cm high and 4 cm wide).



Figure 5: The bent aluminium rod in the frontal (left) and lateral (right) views.

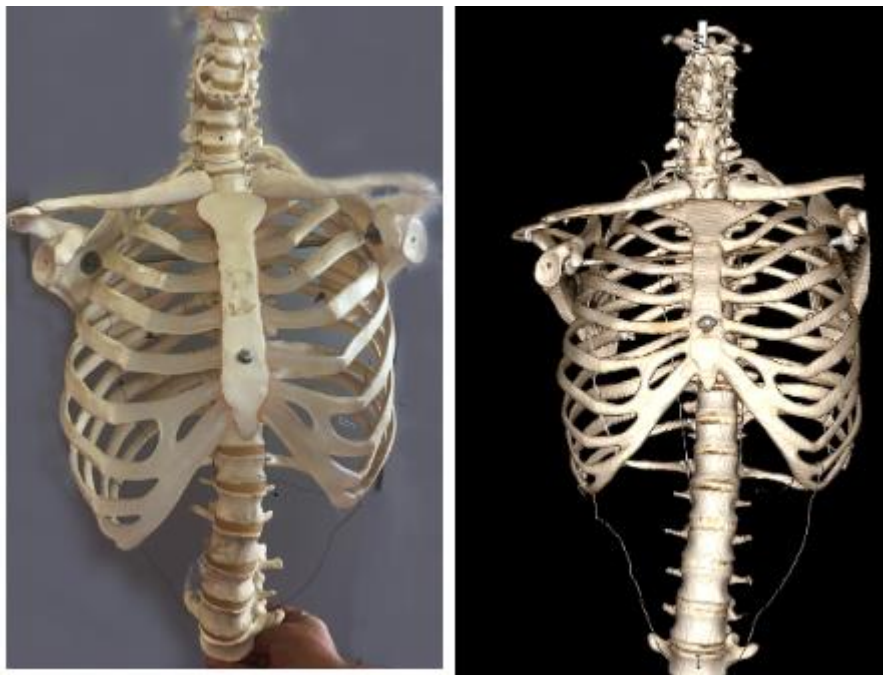


Figure 6: The scoliotic spine model (left) and imaged using a third-generation 16-slice CT scanner (Toshiba Aquilion; Toshiba Medical Systems, Tokyo, Japan) (right).

## **Constructing the phantom**

PMMA slabs are commercially available with various dimensions. Accordingly, the length, width and height of the stack of slabs, and hence the torso size, based on the size of an average 10-year-old girl, and extracted from CT images of a 10-year-old girl, could be constructed to be 50 cm (height), 25 cm (lateral) and 20 cm (deep), respectively. The chest and waist circumferences were 62 cm and 57 cm, respectively, which are within the anatomical reference data.<sup>19-22</sup> The anonymised images of the 10-year-old girl were part of an educational database; therefore, there were no ethical implications.

The research the phantom would be used for was the measurement of Cobb angle using CT scanned projection radiograph (SPR) images. Therefore, the anteroposterior/posteroanterior (AP/PA), and hence coronal, view of the phantom would be acquired to perform the measurements. This was an important consideration for the phantom design, because if the aim would have been to take axial or sagittal CT images, then this could have resulted in image artefacts which would appear as lines in the SPR images created at the interface of adjacent PMMA slabs. Another important consideration for the phantom design was the slab thickness, whereby thin slabs, of 2 mm thickness, were used in the spine area to maintain the anatomical details of each vertebra, and thick slabs, of 10 mm thickness, were used for the remaining areas towards the anterior surface to increase time efficiency in constructing the phantom.

The scaled-down CT images of the scoliotic spine model were printed on A3 paper (29.7 cm × 42 cm) and used as a template for each PMMA slice. Each image was then aligned with its corresponding PMMA slab, and the details were drawn (Figure 7).

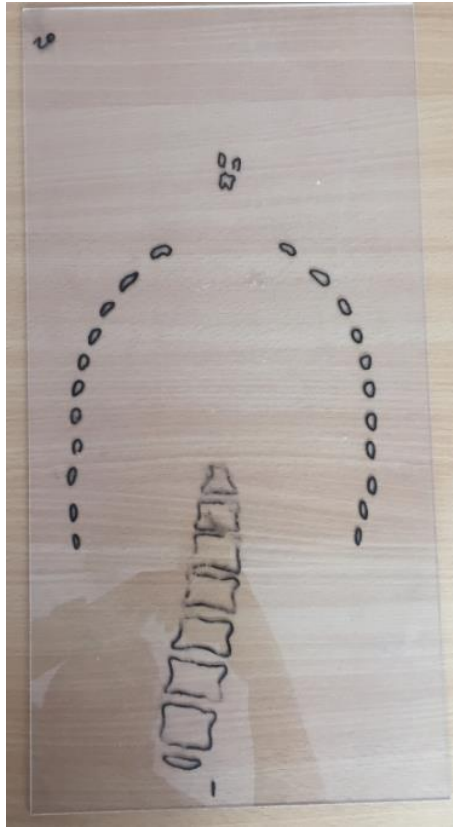


Figure 7: A PMMA slab with the template outline drawn onto it using a pen, ready for drilling.

The outline of the bones and lungs were manually cut out of the slabs (Figure 8), using a hand milling machine, to create compartments to be filled with PoP for bones and air for lungs. The slabs were then combined with each other by stacking every three, to five adjacent slabs together, depending on the formed shape. The edges of the cut-outs in the stacks of slabs were smoothed to improve the accuracy of the anatomical shapes.<sup>23</sup> To keep all the slabs correctly stacked up, they were drilled at all four corners and held together with plastic screws. A further cut-out was added to the slabs in the middle of the phantom at the level of the lumbar spine to house a sheep vertebra to be used in the validation of the phantom. The sheep vertebra was chosen because it shares some structural features with a human vertebra and can be used as an alternative to a human vertebra in radiographic research.<sup>24</sup>

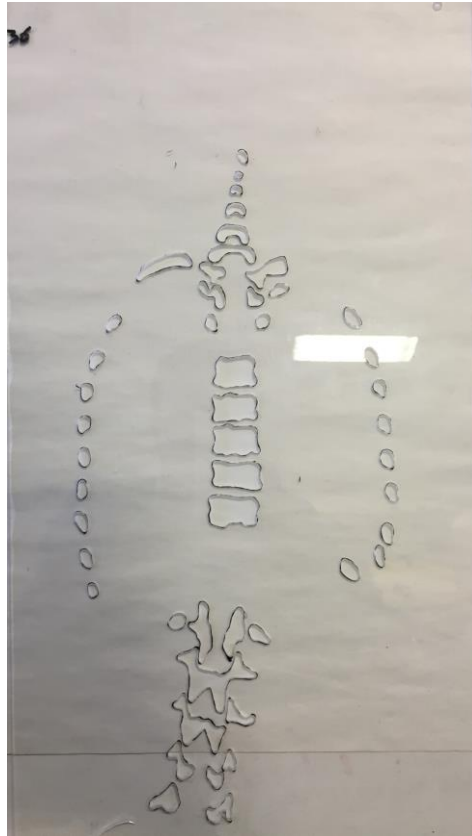


Figure 8: The bony compartments of the ribs and spine cut into one of the PMMA slabs.

The bony compartments in the slabs were then filled with PoP to simulate bone tissue. PoP is a dry powder and must be mixed with water to form a workable paste. The plaster-to-water ratio affects the paste's density in that more water makes the paste less dense.<sup>10,25</sup> To identify the ratio that produces a paste with similar HU to the vertebrae of a 10-year-old girl, several mixtures with different ratios were made and scanned with a CT scanner after they completely dried over a period of 14 days (Table 1). This was long enough for all the water to evaporate from the paste at room temperature and for its HU became constant, as determined by Mohammed Ali *et al.* (2018). Three samples of each mixture were made to ensure the density was accurate.

Table 1: Plaster-to-water ratios used to identify the correct density.
--

Batch	Sample	Water (ml)	Plaster (g)
1	1	20	50
	2	30	50
	3	40	50
2	1	42	50
	2	44	50
	3	46	50
	4	48	50

The HU of the 10-year-old girl's vertebrae was extracted from the CT images.<sup>26-28</sup> Taking into account that vertebrae consist of trabecular and cortical bone tissue, the latter is denser and forms the endplates of the vertebrae. As Cobb angle measurement is performed using vertebral endplates, it was necessary to know the HU of the endplates to ensure the plaster-to-water ratio of the paste has a very similar HU. We calculated that the HU of a 10-year-old girl's vertebral endplates was 598 HU (SD = 79) (Figure 9). The HU of the water-to-plaster ratio of 48:50 was the closest to that of the vertebral endplates.

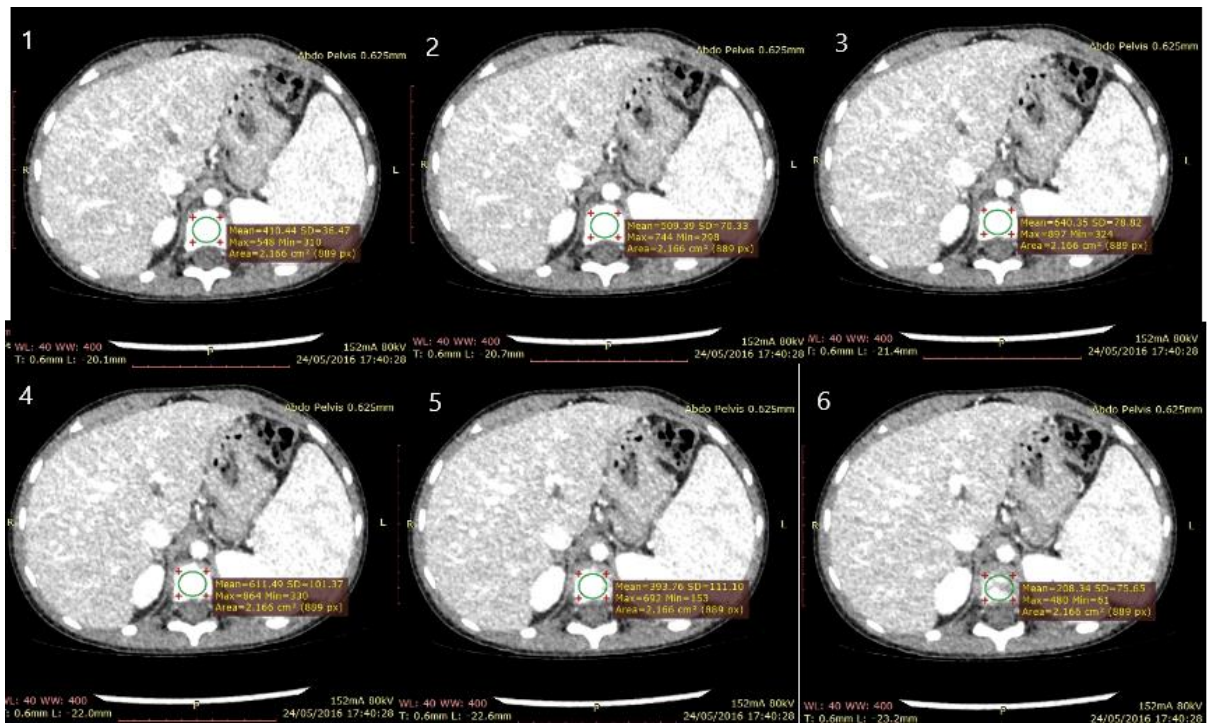


Figure 9: Series of CT scan slices show the variation in the density of a vertebra, using the 10-year-old female CT image data. The series goes from image 1 to image 6, as labelled; images 4 and 5 are at the edge of the vertebra.

Two adjacent slabs were combined in preparation for the PoP filling and weighted down to ensure no PoP leaked between slabs. The PoP powder was prepared in small cups of 50-g portions and mixed with water only when a portion was about to be used for filling. The mixing discontinued when the paste reached the desired consistency, just when it was about to solidify. It was not practical to use a runny mixture because it would go between the slabs, even though they were weighted down. The paste was then ‘pushed’ into the compartments to ensure they were filled, whereby any excess paste was removed so that the paste was flat and flush with the top slab. After that, the paste was left to dry for six days before HU monitoring began. However, the drying was slower than anticipated, because it was more difficult for the water to evaporate due to the combined slabs. Therefore, the slabs were disassembled to expose the set paste, or PoP, to more air and hence speed up the drying process. At day 25, no changes in HU were observed; however, the PoP was left for more than 1 month to ensure

that it was completely dry (Figure 10). Finally, the slabs were reassembled again, and the PoP put back into the slabs.

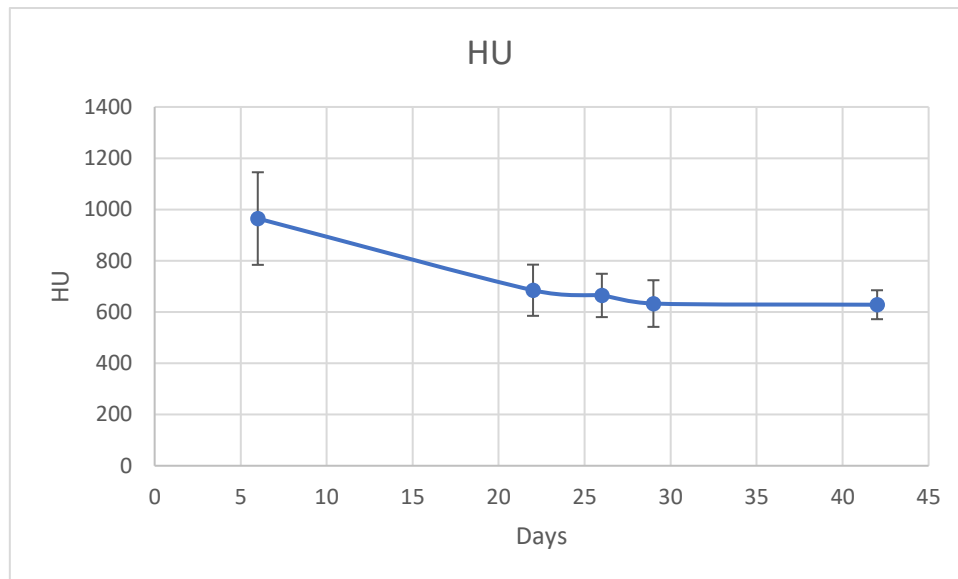


Figure 10: Drying of PoP, with PoP within the phantom.

### Validation of the phantom

The phantom was built to provide a tool for testing the accuracy of Cobb angle measurements when using x-ray imaging machines. However, before experimentation could be carried out on the phantom, it had to be validated for representing the human body and hence fulfilling the purpose for which it had been designed.

The density of the simulated bone in the phantom was compared with that of the spine of a 10-year-old girl. The comparison was made using the HU, an accepted measure for identifying the density of materials.<sup>28,29</sup> because it shows the attenuation characteristics of the materials. Prior irradiating the phantom for HU measurements, the CT scan was checked for the accuracy of HU and the results were within the acceptable tolerance<sup>30,31</sup> The phantom was scanned using CT, with acquisition parameters used were to those for scanning the girl (kVp

=80 and mA = 120), because the HU is affected by the quality of the radiation (i.e. kV).<sup>32</sup>

Bone homogeneity was evaluated using the standard deviation of the HU values. All HU measurements were performed using RadiANT image viewing software (MediAnt, Poznan, Poland).

The phantom was also validated using pixel values. Here, the signal and noise level in the phantom's images were compared with that of a commercially available and validated phantom: a multipurpose ATOM chest phantom (LUNGMAN, Kyoto Kagaku Co., Kyoto, Japan). The phantom represents a male chest torso and has an embedded portion of a synthetic spine (i.e. epoxy resin) that is similar to human bone.<sup>33</sup> The images of the two phantoms were acquired using a DR system (Konica Minolta Medical Imaging, Ramsey, NJ, USA) (Figure 11) at a range of kV and mA values shown in Table 2. The values of kVp were selected based on Local diagnostic reference figures and the selected range of mAs values would cover the possible values of automatic exposure control when irradiating a 10-year old child.

Table 2: The variation of kVp and mAs values used to acquire the two phantom images for SNR calculation

kVp	mAs
75	1
80	2
85	3.2
90	4
95	5
100	6.3
105	7.1
110	8
115	9
120	10
	11
	12.5
	14
	16
	18
	20

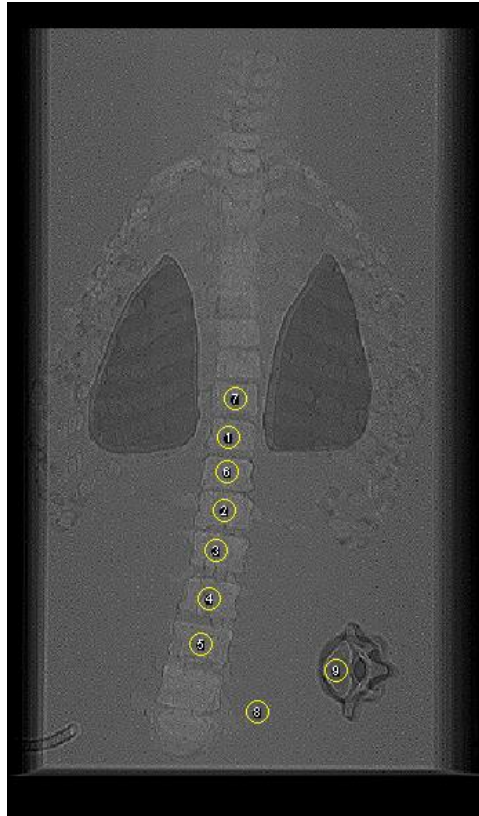


Figure 11: Region of interest (ROI) used to calculate the SNR (signal-to-noise ratio).

Finally, the degree of the curve was measured directly on the phantom to confirm that the angle was  $15^\circ$ . This could be achieved because the PMMA slabs were transparent and the spine was visible. The Cobb angle was then determined manually using a pencil to outline the vertebral endplates and a protractor to measure the angle.

One important part of the Cobb method is identifying the most tilted vertebrae. To do so, all tilted vertebrae are selected, and the Cobb method is performed on all combinations of two vertebrae (e.g. when selecting T5 and T6 as the superior vertebrae, and L1 and L2 as the inferior vertebrae, angle measurements are performed four times, as follows: T5 and L1, T5 and L2, T6 and L1, T6 and L2). Then, the measurements are compared and the pair of vertebrae with the largest angle is selected as the most tilted vertebrae.

## **Data analysis**

All data were tested for normality based on the Shapiro-Wilk test, and p values greater than 0.05 were representing normally distributed data. Consequently, the relationship between the signal-to-noise ratio (SNR) values of the constructed and the LUNGMAN phantoms were analysed using Spearman's correlation test.

## Results

### Validation of the phantom

Table 3 reports the HU for human vertebra, sheep vertebra and PoP vertebra. Table 4 and Table 5 show the relationship between SNR values of the constructed and LUNGMAN phantoms at several kVp and mAs values. Table 4 shows the correlation between the two phantoms at each kVp when changing the mAs values, and Table 5 shows the correlation between the phantoms at each mAs when changing the kVp values. The overall correlation was strong and positive:  $r = 0.93$  ( $p = 0.00$ ). Also, Cobb angle measurement on the phantom confirmed that the constructed curve was  $14^\circ$ . The pairs of vertebrae that formed the angle were T5 and L2, T5 and L3, and T6 and L3. The phantom and its images are shown in Figure 12 Figure 13.

Table 3: Comparison of HU for different bone tissues with the HU of PoP

Vertebra	Real spine (Whole)	Real spine (Edges*)	Sheep (Whole)	Sheep (Edges*)	PoP vertebrae
Average HU	460	598	116	605	628
SD	107	79	155	83	56

\* Refers to the cortical part of the vertebrae.

Table 4: The correlation between SNR values of constructed and LUNGMAN phantoms at several kVp values when changing mAs values.

kVp	Spearman's correlation	p-value
75	0.99	0.00
80	0.99	0.00
85	0.99	0.00
90	0.97	0.00
95	0.95	0.00
100	0.97	0.00
105	0.97	0.00
110	0.97	0.00
115	0.72	0.00
120	0.91	0.00

Table 5: The correlation between SNR values of constructed and LUNGMAN phantoms at several mAs values when changing kVp values.

mAs	Pearson correlation	p-value
1	0.88	0.00
2	0.88	0.00
3.2	0.97	0.00
4	0.95	0.00
5	0.96	0.00
6.3	0.97	0.00
7.1	0.99	0.00
8	0.90	0.00
9	0.98	0.00
10	0.98	0.00
11	0.95	0.00
12.5	0.99	0.00
14	0.94	0.00
16	0.96	0.00
18	0.97	0.00
20	0.97	0.00

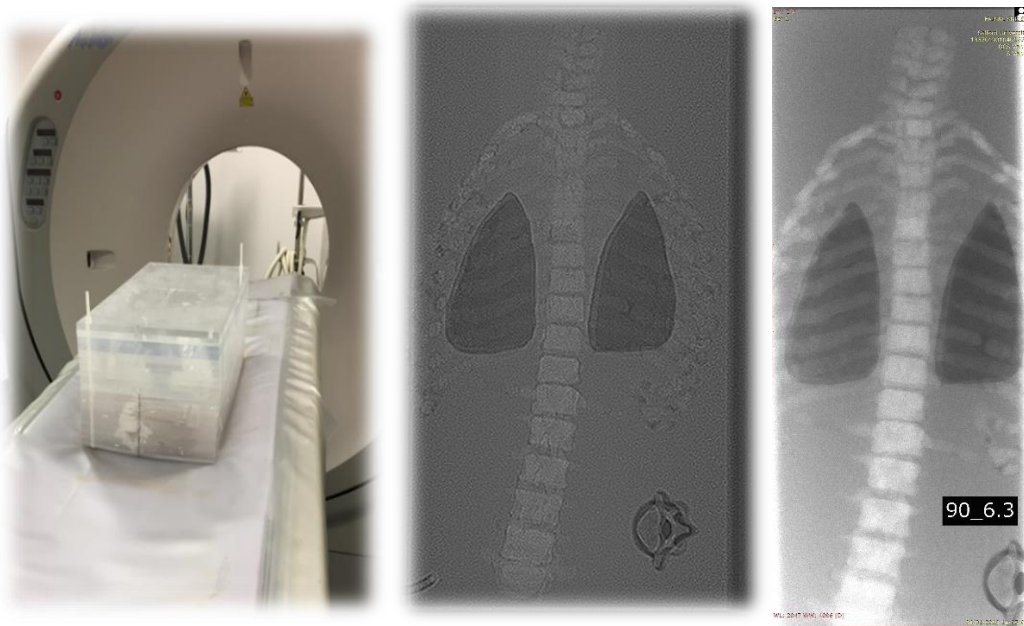


Figure 12: The phantom on the CT table (left); an AP projection image of the phantom acquired using SPR mode (middle); and an AP view image acquired using the DR.



Figure 13: A 3D image of the phantom

## Discussion

Attempts have been undertaken to develop new x-ray imaging machines and imaging protocols to minimise the radiation risk to patients with AIS. In the published studies that have optimised AIS imaging techniques, phantoms with normal spine were used, and finding the optimum image quality was based on evaluating image quality rather than testing the accuracy of Cobb angle measurements,<sup>34-36</sup> which cannot be used to test the accuracy of the measurements. The aim of our work was to build a phantom which could be used for testing the accuracy of Cobb angle measurements and optimising AIS imaging.

The human body contains several types of tissue that interact differently with X-ray photons. Therefore, the phantom should not only mimic the size and shape of the human body<sup>33</sup> but should have materials with photon mass attenuation and mass absorption coefficients similar to that of human tissue.<sup>37,38</sup> PMMA and PoP were chosen to build our phantom because PMMA is commonly used as a soft tissue substitute in diagnostic radiology studies,

especially for non-dosimetry phantoms;<sup>39-47</sup> and it has similar physical properties to soft tissues. It has a mass attenuation coefficient ( $\mu/\rho$ ) similar to that of soft tissue in the diagnostic energy range;<sup>48,49</sup> and PoP has mass attenuation coefficient similar to that of bone<sup>49</sup>. Both materials are inexpensive and easy to use and hence, suitable for this study due to its budget and time constraints.

The constructed phantom has the physical characteristics (in terms of spinal deformity) and radiological characteristics (in terms of HU and SNR values) of a 10-year-old child with AIS. The phantom was validated against a phantom that has been widely used in dose optimisation, and a strong correlation was observed. This phantom permits testing of Cobb angle measurement accuracy. Our phantom can also be used for dose optimisation work, to determine the optimum imaging protocol that provides the most accurate Cobb angle measurements while reducing radiation dose to patients.

Our phantom is constructed from low-cost materials. The cost of building the phantom was less than £200, excluding labour. In comparison, commercially available, phantoms designed for radiological studies can cost £10,000 or more, and normally these have a normal straight spine.

An alternative method for constructing a phantom could be 3D printing. Although this approach is still under development, the technology is promising for phantom production. The technology has enabled researchers to produce phantoms with specific purposes in mind and they can include pathologies<sup>50,51</sup>. However, the process of constructing a phantom using 3D printers can be complex and is currently expensive<sup>52-54</sup>. The technology is capable of mimicking the geometry of the human body accurately; however, the materials used to produce the phantoms are still not tissue equivalent materials<sup>50,53,55</sup>.

Although our phantom represented the spine of patients with AIS very well, it is not, however, without limitations. First, its design does not allow for the acquisition of lateral images due to the configuration of the PMMA slabs producing significant artefacts. Second, the PMMA and PoP have a uniform representation of soft tissue and bone, respectively, which does not reflect the nature of the human body. The geometry of the phantom may not be similar to the geometry of human in reality, which is complex and cannot be replicated using the inexpensive materials used in our work. For instance, we used an approximate shape for the lungs to ensure the presence of air inside the phantom. Finally, the phantom does not include the pelvis region, which could have an impact on scatter within the image. The inclusion of the pelvis in the phantom is suggested for future work.

## **Conclusion**

We constructed and validated a phantom with a scoliotic spine using commercially available materials. The phantom was relatively cheap to construct compared to commercially available models. It does lack the anatomical detail that is visible in other phantoms, but it is suitable to be used in dose / image quality optimisation research which investigates new x-ray imaging techniques and technology for the assessment of scoliosis and to optimise currently used protocols.

## References

1. Konieczny MR, Senyurt H, Krauspe R. Epidemiology of adolescent idiopathic scoliosis. *J Child Orthop*. 2013;7(1):3–9.
2. Blevins K, Battenberg A, Beck A. The management of scoliosis. *Adv Pediatr* [Internet]. 2018;65(1):249–66. Available from: <https://doi.org/10.1016/j.yapd.2018.04.013>
3. Heary RF, Albert TJ. [ *Spinal Deformities: The Essentials* ]. 2 nd. New York: Thieme; 2014.
4. Kim W, Porrino JA, Hood KA, Chadaz TS, Klauser AS, Taljanovic MS. Clinical Evaluation, Imaging, and Management of Adolescent Idiopathic and Adult Degenerative Scoliosis. *Curr Probl Diagn Radiol* [Internet]. 2018;000:1–13. Available from: <https://linkinghub.elsevier.com/retrieve/pii/S0363018818302196>
5. Presciutti SM, Karukanda T, Lee M. Management decisions for adolescent idiopathic scoliosis significantly affect patient radiation exposure. *Spine J* [Internet]. 2014;14(9):1984–90. Available from: <http://dx.doi.org/10.1016/j.spinee.2013.11.055>
6. National Research Council. *Analysis of Cancer Risks in Populations Near Nuclear Facilities: Phase 1* [Internet]. Washington, DC: The National Academies Press; 2012. Available from: <https://www.nap.edu/catalog/13388/analysis-of-cancer-risks-in-populations-near-nuclear-facilities-phase>
7. Carpenter DO, Bushkin-Bedient S. Exposure to chemicals and radiation during childhood and risk for cancer later in life. *J Adolesc Heal* [Internet]. 2013;52(5 SUPPL):S21–9. Available from: <http://dx.doi.org/10.1016/j.jadohealth.2013.01.027>

8. Shuryak I, Hahnfeldt P, Hlatky L, Sachs RK, Brenner DJ. A new view of radiation-induced cancer: Integrating short- and long-term processes. Part II: Second cancer risk estimation. *Radiat Environ Biophys*. 2009;48(3):275–86.
9. Chung N, Cheng YH, Po HL, Ng WK, Cheung KC, Yung HY, et al. Spinal phantom comparability study of Cobb angle measurement of scoliosis using digital radiographic imaging. *J Orthop Transl [Internet]*. 2018;15:81–90. Available from: <https://doi.org/10.1016/j.jot.2018.09.005>
10. Mohammed Ali A, Hogg P, Johansen S, England A. Construction and validation of a low cost paediatric pelvis phantom. *Eur J Radiol [Internet]*. 2018;108(September):84–91. Available from: <https://linkinghub.elsevier.com/retrieve/pii/S0720048X18303206>
11. Soucacos P, Zacharis K, Beris A, Xenakis A, Greece J. School-Screening for Scoliosis. *J Bone Jt Surg*. 1997;1498–503.
12. Wong H-K, Hui JHP, Rajan U, Chia H-P. Idiopathic scoliosis in Singapore schoolchildren: a prevalence study 15 years into the screening program. *Spine (Phila Pa 1976)*. 2005;30(10):1188–96.
13. Kamtsiuris P, Atzpodien K, Ellert U, Schlack R, Schlaud M. Prävalenz von somatischen Erkrankungen bei Kindern und Jugendlichen in Deutschland. *Bundesgesundheitsblatt - Gesundheitsforsch - Gesundheitsschutz [Internet]*. 2007;50(5–6):686–700. Available from: <http://link.springer.com/10.1007/s00103-007-0230-x>
14. Cilli K, Tezeren G, Tas T, Bulut O, Ozturk H, Oztemur Z, et al. School screening for scoliosis in Sivas, Turkey Kansu. *Acta Orthop Traumatol Turc*. 2009;43(5):426–30.
15. Nery LS, Halpern R, Nery PC, Nehme KP, Stein AT. Prevalence of scoliosis among

- school students in a town in southern Brazil. *Sao Paulo Med J.* 2010;128(2):69–73.
16. Suh SW, Modi HN, Yang JH, Hong JY. Idiopathic scoliosis in Korean schoolchildren: A prospective screening study of over 1 million children. *Eur Spine J.* 2011;20(7):1087–94.
  17. Ueno M, Takaso M, Nakazawa T, Imura T, Saito W, Shintani R, et al. A 5-year epidemiological study on the prevalence rate of idiopathic scoliosis in Tokyo: School screening of more than 250,000 children. *J Orthop Sci.* 2011;16(1):1–6.
  18. Adobor RD, Rimeslatten S, Steen H, Brox JI. School Screening and Point Prevalence of Adolescent Idiopathic Scoliosis in 4000 Norwegian Children Aged 12 Years. *Scoliosis Spinal Disord J.* 2011;6(1):23.
  19. Kuba VM, Leone C, Damiani D. Is waist-to-height ratio a useful indicator of cardio-metabolic risk in 6-10-year-old children? *BMC Pediatr.* 2013 Jun;13:91.
  20. Showalter CK, White DR, Williams G, Wilson IJ, Buckland-Wright JC, Rothenberg LN, et al. Phantoms and Computational Models in Therapy, Diagnosis and Protection (Report 48) [Internet]. *Journal of the International Commission on Radiation Units and Measurements.* Bethesda, Maryland; 1992 Apr. Available from: <https://doi.org/10.1093/jicru/os25.1.Report48>
  21. ICRP. Basic Anatomical and Physiological Data for Use in Radiological Protection Reference Values [report 89]. *Ann ICRP* [Internet]. 2002;32(3):3–4. Available from: <http://www.sciencedirect.com/science/article/pii/S0146645303000022>
  22. Mertz HJ, Jarrett K, Moss S, Salloum M, Zhao Y. The Hybrid III 10-Year-Old Dummy. *Stapp Car Crash J.* 2001 Nov;45:319–28.

23. Mohammed Ali A. An Investigation into Methods for Dose Optimisation for Paediatric AP Pelvis Projections When Considering Size Variations. University of Salford; 2019.
24. Sheng S-R, Wang X-Y, Xu H-Z, Zhu G-Q, Zhou Y-F. Anatomy of large animal spines and its comparison to the human spine: a systematic review. *Eur Spine J* [Internet]. 2009/10/30. 2010 Jan;19(1):46–56. Available from: <https://www.ncbi.nlm.nih.gov/pubmed/19876658>
25. Madu MJ, Ndaliman, Oche B. Evaluation of Water-to-Plaster Ratio on Products of Nafada Plaster of Paris (POP). *Int J Emerg Eng Res Technol Int J Emerg Eng Res*. 2016;4(10).
26. Gücük A, Uyetürk U. Usefulness of hounsfield unit and density in the assessment and treatment of urinary stones. *World J Nephrol* [Internet]. 2014/11/06. 2014 Nov 6;3(4):282–6. Available from: <https://www.ncbi.nlm.nih.gov/pubmed/25374823>
27. Homolka P, Gahleitner A, Prokop M, Nowotny R. Optimization of the composition of phantom materials for computed tomography. *Phys Med Biol* [Internet]. 2002;47(16):2907–16. Available from: <http://dx.doi.org/10.1088/0031-9155/47/16/306>
28. Homolka P, Nowotny R. Production of phantom materials using polymer powder sintering under vacuum. *Phys Med Biol*. 2002 Feb;47(3):N47-52.
29. Mattsson S, Thomas BJ. Development of methods for body composition studies. *Phys Med Biol*. 2006 Jul;51(13):R203-28.
30. CEC. European guidelines on quality criteria for computed tomography. Report EUR 16262 EN. Luxembourg: Office for Official Publications of the European Communities; 1996.

31. Cropp RJ, Seslija P, Tso D, Thakur Y. Scanner and kVp dependence of measured CT numbers in the ACR CT phantom. *J Appl Clin Med Phys*. 2013;14(6):338–49.
32. Zurl B, Tiefling R, Winkler P, Kindl P, Kapp KS. Hounsfield units variations. *Strahlentherapie und Onkol [Internet]*. 2014;190(1):88–93. Available from: <https://doi.org/10.1007/s00066-013-0464-5>
33. Dewerd LA, Kissick M. *The phantoms of medical and health physics*. 2014.
34. Ernst C, Buls N, Laumen A, Van Gompel G, Verhelle F, de Mey J. Lowered dose full-spine radiography in pediatric patients with idiopathic scoliosis. *Eur Spine J [Internet]*. 2018;27(5):1089–95. Available from: <https://doi.org/10.1007/s00586-018-5561-9>
35. Hensen J, Jurik AG, Fiirgaard B, Egund N. Optimisation of scoliosis examinations in children. *Pediatr Radiol*. 2003;33(11):752–65.
36. Geijer H, Verdonck B, Beckman K-W, Andersson T, Persliden J. Digital radiography of scoliosis with a scanning method: radiation dose optimization. *Eur Radiol [Internet]*. 2003;13(3):543–51. Available from: <http://www.ncbi.nlm.nih.gov/pubmed/12594558>
37. Watanabe Y, Constantinou C. Phantom material for radiology. In: *Encyclopedia of Medical Devices and Instrumentation*. John Wiley&Sons; 2006.
38. White DR, Constantinou C. Anthropomorphic Phantom Materials BT - Progress in Medical Radiation Physics. In: Orton CG, editor. Boston, MA: Springer US; 1982. p. 133–93. Available from: [https://doi.org/10.1007/978-1-4615-7691-4\\_3](https://doi.org/10.1007/978-1-4615-7691-4_3)
39. Chambers D, Bohay R, Kaci L, Barnett R, Battista J. The effective dose of different scanning protocols using the Sirona GALILEOS® comfort CBCT scanner. *Dentomaxillofacial Radiol*. 2015;44(2).

40. Koivisto J, Kiljunen T, Wolff J, Kortensniemi M. Characterization of MOSFET dosimeter angular dependence in three rotational axes measured free-In-Air and in soft-Tissue equivalent material. *J Radiat Res.* 2013;54(5):943–9.
41. Sossin A, Rebuffel V, Tabary J, Létang JM, Freud N, Verger L. Characterizing the behavior of scattered radiation in multi-energy x-ray imaging. 2017 [cited 2019 Mar 21]; Available from: <http://dx.doi.org/10.1016/j.nima.2017.01.032>
42. Yvert M, Diallo A, Bessou P, Rehel JL, Lhomme E, Chateil JF. Radiography of scoliosis: Comparative dose levels and image quality between a dynamic flat-panel detector and a slot-scanning device (EOS system). *Diagn Interv Imaging* [Internet]. 2015;96(11):1177–88. Available from: <http://dx.doi.org/10.1016/j.diii.2015.06.018>
43. McCullagh JB, Baldelli P, Phelan N. Clinical dose performance of full field digital mammography in a breast screening programme. *Br J Radiol* [Internet]. 2011 Nov;84(1007):1027–33. Available from: <https://www.ncbi.nlm.nih.gov/pubmed/21586506>
44. Lofthag-Hansen S. Cone beam computed tomography radiation dose and image quality assessments. *Swed Dent J Suppl.* 2010;(209):4–55.
45. Chung E, Seuntjens J, Soisson E, Bouchard H. Advanced dosimetry techniques for accurate verification of non-standard beams [Internet]. International Atomic Energy Agency (IAEA); 2010. Available from: [http://inis.iaea.org/search/search.aspx?orig\\_q=RN:42026442](http://inis.iaea.org/search/search.aspx?orig_q=RN:42026442)
46. Barnes PJ, Temperton D. Compliance of Full Field Digital Mammography Systems with the European Protocol for Image Quality and Dose [Internet]. International Atomic Energy Agency (IAEA); IAEA; 2011. Available from: <http://www->

pub.iaea.org/MTCDD/Publications/PDF/P1514\_web/p1514\_vol2\_web.pdf

47. Garcia T, Perichon N, Lourenco V, Bordy JM, Francois P. Calibration of helical tomotherapy using ESR/alanine dosimetry [Internet]. International Atomic Energy Agency (IAEA); 2010. Available from:  
[http://inis.iaea.org/search/search.aspx?orig\\_q=RN:42026513](http://inis.iaea.org/search/search.aspx?orig_q=RN:42026513)
48. Russo P. Physical basic of X-ray imaging. In: Comprehensive Biomedical Physics. 1st ed. Elsevier; 2014.
49. Hubbell JH, Seltzer SM. Tables of X-Ray Mass Attenuation Coefficients and Mass Energy-Absorption Coefficients (version 1.4). National Institute of Standards and Technology. 2004.
50. Hazelaar C, van Eijnatten M, Dahele M, Wolff J, Forouzanfar T, Slotman B, et al. Using 3D printing techniques to create an anthropomorphic thorax phantom for medical imaging purposes. *Med Phys*. 2018 Jan;45(1):92–100.
51. Mitsouras D, Liacouras P, Imanzadeh A, Giannopoulos AA, Cai T, Kumamaru KK, et al. Medical 3D Printing for the Radiologist. *Radiographics*. 2015;35(7):1965–88.
52. Squelch A. 3D printing and medical imaging. Vol. 65, *Journal of medical radiation sciences*. United States; 2018. p. 171–2.
53. Kim M-J, Lee S-R, Lee M-Y, Sohn JW, Yun HG, Choi JY, et al. Characterization of 3D printing techniques: Toward patient specific quality assurance spine-shaped phantom for stereotactic body radiation therapy. *PLoS One*. 2017;12(5):e0176227.
54. Filippou V, Tsoumpas C. Recent advances on the development of phantoms using 3D printing for imaging with CT, MRI, PET, SPECT, and ultrasound. *Med Phys*.

2018;45(9):e740–60.

55. Solc J, Vrba T, Burianova L. Tissue-equivalence of 3D-printed plastics for medical phantoms in radiology. *J Instrum.* 2018;13(9).